MTLA 34 (2024) 102083

Contents lists available at ScienceDirect

Materialia

journal homepage: www.elsevier.com/locate/mtla

Architecting strength: Innovative microstructural design of Aluminum/Alumina Nanocomposites via cold-welded flaky-shaped particles and pressure-assisted sintering

Behzad Sadeghi [a], Behzad Sadeghian [b], Pasquale Cavaliere [a,*], Aboozar Taherizadeh [b]

[a] Department of Innovation Engineering, University of Salento, Via per Arnesano, 73100 Lecce, Italy
[b] Department of Materials Engineering, Isfahan University of Technology, Isfahan 84156-83111, Iran

ARTICLE INFO

Key words:
Al/Al_2O_3 composites
Architecture
Cold welding
Al_2O_3 distribution
Strain hardening

ABSTRACT

Aluminum/alumina (Al/ Al_2O_3) nanocomposites with three different microstructural architectures were prepared using flake powder metallurgy, which involves the conversion of spherical Al powder into nanoflakes by ball milling, the introduction of Al_2O_3 by natural oxidation, the control of the powder microstructure by cold welding, and then powder by densification, sintering, and extrusion. The experimental results showed that the shape of the Al matrix grains and the distribution of native Al_2O_3, the so-called Al/Al_2O_3 architectures, could be precisely controlled by BM. The nanolaminate architecture, in which the Al_2O_3 nanoplatelets were aligned along the boundaries of lamellar or elongated grains, exhibited a more balanced combination of tensile strength and ductility than the random architecture with non-uniformly distributed Al_2O_3 nanoplatelets within equiaxed grains. This improvement can be attributed to the combined effect of higher Al_2O_3 strengthening efficiency and better work hardening ability. The research results suggest that the presence of Al_2O_3 nanoplatelets at high-angle grain boundaries significantly hinders the main mechanism of subgrain rotation for the formation of new boundaries. Moreover, the simulation accurately predicts the higher degree of grain faceting in finer-grained samples, which is consistent with the experimental data indicating more pronounced hexagonal grain shapes. Consequently, flake powder metallurgy offers a promising approach for the production of strong and ductile Al-matrix composites through the design of their microstructural architecture.

1. Introduction

Particle-reinforced Al matrix composites (PRAMCs) are in high demand in the high-tech sector due to their low weight, superior strength and high modulus [1,2]. By refining the grains of the Al matrix into the submicron range (Ultrafine Grain, UFG) or into the nanoscale (Nano Grain, NG), the strength of PRAMCs is significantly improved compared to those with coarse grains [3,4]. In addition, the severe thermal mismatch between particles and matrix, which usually leads to poor elongation and low fracture toughness in conventional metal matrix composites, cannot occur in UFG/NG PRAMCs [1,5]. However, UFG/NG-PRAMCs have the same problem as UFG/NG metals, namely the relatively low ductility resulting from the lack of strain hardening and increased dynamic recovery in the fine grains [3,6,7].

The number of publications on the design of the microstructural architecture of Al/Al_2O_3 nanocomposites using powder metallurgy indicates a growing interest in this field. The number of published articles has steadily increased over the years, highlighting the importance of this field of research. In particular, research is being carried out into how the microstructural architecture influences the mechanical properties, especially the strength/ductility ratio. To solve this dilemma, various strategies have been applied, such as bimodal structure, nano-sized twins, intragranular nano-dispersoids and gradient structure [6, 8-12]. It is reported that the microstructure of Al_2O_3/Al composites can be tailored by controlling the powder properties, processing techniques and sintering conditions [11,12]. The microstructural architecture has a significant effect on the mechanical properties, and optimization is crucial to improve the performance of Al_2O_3/Al composites.

All these methods focused on the hierarchical architectural design of the material to promote dislocation activity and improve work hardening ability. Recently, a biomimetic nanolaminated nanocomposite of 6 wt% Al/Al_2O_3 was prepared by Jiang et al. [13] using a newly

* Corresponding author.
E-mail address: pasquale.cavaliere@unisalento.it (P. Cavaliere).

https://doi.org/10.1016/j.mtla.2024.102083
Received 16 January 2024; Accepted 8 April 2024
Available online 8 April 2024

developed flake powder metallurgy (FPM). Sadeghi et al. [14] also utilized micro/macro rolling (MMR) to produce laminated Al_2O_3/Al composites with high dislocation storage capacity. In both studies, it was shown that the elongated Al grains with high aspect ratio were sandwiched by two Al_2O_3 layers. The Al_2O_3 platelets at the lamellar interface were originally formed on the surface of the Al nanoflake powders by natural oxidation during material processing. The Al/Al_2O_3 nanocomposite exhibited a superior strength of 262 MPa and an overall elongation of 22.9 %, which was comparable to that of the 15 wt% Al/Al_2O_3 nanocomposite prepared by the friction stir process (FSP) [15–17]. Recently, effective and feasible strategies for uniform dispersion of a high proportion of nanoparticles in nanoflake powder were proposed by a flake design strategy in which the particles are dry coated [18,19]. However, all these research works focused on the preparation of powders and paid no attention to the solid state of these composites. Despite the great effect, the underlying reinforcement and toughening mechanisms in the biomimetic nanolaminate structure are still unknown. This research fills this gap by systematically analyzing different microstructural architectures and their influence on the mechanical response of the composites. The novelty of this study lies in the comprehensive exploration of the influence of microstructural architecture on the mechanical properties of Al/Al_2O_3 composites. While previous research focused on the reinforcement aspect, this work systematically investigates how the specific arrangement of Al_2O_3 nanoparticles in the composite matrix affects the tensile strength, ductility and strain- hardening behavior. This quantitative analysis allows a rigorous evaluation of the architectural variations and their impact on material performance. In addition, the study addresses the role of cold welding in shaping microstructural development and highlights the effects of plastic deformation on the resulting architecture and properties. By uncovering the interactions between dislocations and Al_2O_3 nanoplatelets, the research reveals the underlying mechanisms that control strain hardening, plastic instability and overall mechanical behavior. Although there are parallels with previous work, this study stands out in that it provides new insights into the role of nanoplatelet arrangement, deformation mechanisms and their combined effects on composite material design.

Therefore, this study focuses on dictating the architecture of Al/Al_2O_3 to investigate the structural effect, strengthening and toughening mechanisms of the laminated structure. By cold welding the Al nanoflake powders, the morphology and distribution of Al_2O_3 platelets as well as the mesoscopic structural features (nanolaminated, random and mixed) in the final Al/Al_2O_3 nanocomposite can be well controlled. The microstructure evolution and mechanical performance of the Al/Al_2O_3 nanocomposite are well studied. Through analytical calculations, the strengthening efficiency of the Al_2O_3 flakes and strain hardening of the final composites are compared between the samples with different architectures. In addition, to illustrate the flexibility and efficiency of the flake design concept in the consolidation step, the process of sintering the flakes was simulated using FEM simulation. Since no report has been found so far using nanoflake powders as host particles to produce composite particles by the technology of dry particle coating followed by consolidation, this paper first investigates the flexibility of the flake design concept in incorporating deformations that occur simultaneously with the compaction rate, considering the active mechanisms involved. The experimental results show that the nanoaminated structure has the highest strength efficiency of the Al_2O_3 flakes and the best consolidation ability. The whole study provides new processing possibilities and theoretical guidance for designing the architecture of metallic materials.

2. Experiments

2.1. Sample preparation

Al/Al_2O_3 composites were prepared using powder metallurgy techniques, particularly by controlling the cold welding (CW) step. In this process, spherical aluminum powder with a purity of 99.9 % and an average particle size of 10 μm was used as the starting material. To produce flaked aluminum powder, slow ball milling in a planetary BM is used under various processing conditions, such as milling time and rotation speed. In our preliminary experiments [14,20,21], a rotation speed of 190 rpm at 3 hour (h) can provide the conditions required for our study, namely the production of flakes with a thickness of about 500 nm.

In order to achieve different microstructural architectures in the final Al/Al_2O_3 composite, the flaky powders obtained from 3 h of BM were subjected to additional 15 min, 1 h, and 2 h of BM (referred to as cold welding) at a ball to powder weight ratio of 20:1 and a rotation speed of 450 rpm under an argon atmosphere. To prevent excessive welding of the milled aluminum powder, 2 wt% stearic acid was added to the mixture. In addition, the BM was performed with an interim period of 1 h for every 7 min in order to prevent the over-heating behavior. Subsequently, all three sets of powders, namely 15 min, 1 h and 2 h, were fully solidified by hot pressing at 500 °C and 500 MPa for 2 h. They were then sintered at 550 °C for 2 h and extruded at 500 °C with an extrusion ratio of 20:1 to form a 10 mm thick rod. Finally, the samples were compacted by hot rolling, reducing the thickness by 50 % at 150 °C in certain passes.

2.2. Microstructure characterization

The Al_2O_3 phase in the composite was analyzed by X-ray diffraction (XRD; Rigaku and CN2301) with a Cu Ka radiation source. The chemical compositions of the flake powders and the extrusion rods were analyzed by inductively coupled plasma optical emission spectroscopy to determine the proportion of oxide layers. The morphology of the ball-milled powder, which varied depending on the milling intensity and time, was observed using a field emission scanning electron microscope (SEM, FEI Quanta FEG 250) or a high-resolution TEM (HRTEM, JEOL 2000). EBSD (electron backscattered diffraction) analyzes were performed at a step size of 100 nm using a JEOL JSM-7001F SEM (Tokyo, Japan) at 15 kV. Microstructural analysis of the extruded samples was performed by TEM to gain insight into the effects of cold-welding time on the structural evolution of the material. The TEM images were acquired for three different cold-welding times: 15 min, 1 h and 2 h. The samples were carefully prepared for TEM analysis by Ar-beam ion milling on the GATAN PIPS II machine to obtain thin sections suitable for high-resolution images. Grain diameters were estimated by measuring and averaging the length and width of the grains in bright field TEM images of an area of 225 μ,m-2. For statistical analysis, the grain size of approximately 300 grains per sample was measured using ImageJ software. To complement the microstructural analysis, energy dispersive X-ray spectroscopy (EDS, SuperX detector) was used to map the distribution of Al_2O_3 nanoplatelets within the grains. Phase identification was performed by X-ray diffraction (XRD, XRD- 600, Shimadzu, Japan, Cu Kα, 2° min^{-1}). In addition, XRD and EBSD analyzes were performed to investigate the deformation texture of the extruded samples. The XRD analysis, especially using the William-Hall method, confirmed the more active interaction of dislocations in the 0-h cold weld sample (320 nm). For this purpose, the dislocation density of the samples was calculated using [22]

$$\rho = \left(3\sqrt{2\pi}\,\varepsilon^{2^{1/2}}\right)\Big/(D\mathrm{b}) \tag{1}$$

Where D is the equivalent average grain size estimated from TEM images, $\varepsilon^{2^{1/2}}$ is the micro strain, ρ is the dislocation density, b is Burgers vector of Al, which is 0.286 nm [23].

2.3. Tensile behavior

The tensile tests were performed at room temperature using a mechanical universal testing machine (AUTOGRAPH AG-I 50 kN,

Shimadzu, Japan). For each condition, at least three tests were performed at a strain rate of 5 × 10–4. The Al/Al_2O_3 composites with different cold-welding times as the main processing parameters are referred to as CW-15 min, CW-1 h and CW-2 h specimens in the following.

2.4. Theory and method

In this section, an elastic phase field model for pressure-assisted sintering is used to simulate the process of sintering flakes. The model accounts for deformations that occur simultaneously with the compaction rate, taking into account the active mechanisms involved. In this model, the density functional is divided into two components: the chemical free energy density, denoted as

f_{ch}, and the elastic energy density, denoted as f_{el}.

The model according to Eq. (1) [24] uses two types of field variables to represent the microstructure. The first variable is the conserved density field, denoted as ρ, which has a value of one in the solid phase and zero in the pores. At the interface between the solid and the pores, it is subject to rapid changes. The second variable is the non-conserved order parameter, denoted η_i, which is used to distinguish between different particles within the microstructure. It takes the value one for a particular particle and zero for other particles. The order parameters not obtained exhibit smooth transitions at the evolving grain boundaries, gradually shifting from one to zero or from zero to one. The representation of the microstructure using these field variables makes it possible to describe the free energy function of the system.

$$F = \int_V f_{ch}(\rho,\eta_i) + \frac{\kappa_\rho}{2}(\nabla\rho)^2 + \sum_i \frac{\kappa_{\eta_i}}{2}(\nabla\eta_i)^2 + f_{el})dV \tag{2}$$

The gradient energy coefficients for concentration and grain boundary energies are denoted as κ_ρ and κ_{η_i}, respectively. These coefficients determine the contribution of gradient effects to the energy of the system. The chemical free energy function, represented as $f_{ch}(\rho,\eta_i)$ in Eq. (2) [25], is approximated using a Landau-type polynomial potential. This approximation allows for an effective characterization of the chemical free energy within the model.

$$f_{ch}(\rho,\eta_i) = A\rho^2(1-\rho)^2 + B\left[\rho^2 + 6(1-\rho)\sum_i \eta_i^2 - 4(2-\rho)\sum_i \eta_i^3 + 3\left(\sum_i \eta_i^2\right)^2\right] \tag{3}$$

The constants A and B are utilized in the potential function. This potential leads to an equilibrium value of mass density, where $\rho = 1$ corresponds to the solid particles, and $\rho = 0$ corresponds to the pores. Similarly, for the multicomponent non-conserved order parameters ηi, they also approach zero at the pores. The potential function ensures that the values of these variables align with the desired states within the microstructure.

The evolution equation governing the behavior of the conserved density field, ρ, is described by the Cahn-Hilliard equation according to Eq. (3) [26]:

$$\frac{\partial\rho}{\partial t} = \nabla.\left(D\frac{\delta F}{\delta\rho}\right) \tag{4}$$

where, the microstructure-dependent diffusivity/mobility coefficient, D, in the Cahn-Hilliard equation, accounts for the diverse diffusion paths that occur throughout the sintering process. Its specific form is assumed to be as Eq. (4) [25,27]:

$$D = D_{vol}\ \varphi(\rho) + D_{vap}\ [1-\varphi(\rho)] + D_{surf}\ \rho\ (1-\rho) + D_{GB}\sum_i\sum_{i\neq m}\eta_i\eta_m \tag{5}$$

In the given equation, D_{vol} represents the diffusivity within the lattice, D_{vap} denotes the diffusivity of the vapor phase, D_{surf} represents the surface diffusivity, and D_{GB} corresponds to the diffusivity at the grain boundary. The interpolation function, φ(ρ), used in the Eq. (4) is assumed to be as Eq. (6) [25,27]:

$$\varphi = \rho^3\ \left(10 - 15\rho + 6\rho^2\right) \tag{6}$$

This guarantees that the diffusion rate is effectively zero within the pore spaces and reaches its highest value within the solid regions.

The Allen-Cahn equation governs the evolution of the non-conserved order parameters η_i, which represent both particles and grain boundaries.

$$\frac{\partial\eta_i}{\partial t} = L\frac{\delta F}{\delta\eta_i} \tag{7}$$

where L is the grain boundary mobility.

The above equations were employed to simulate the sintering effect caused by the pressure between two flakes. Therefore, the calculation of the elastic strain energy density within the contact is performed using Eq. (7) [24,28]:

$$f_{el} = \int_V \frac{\Omega_{ij}}{\Omega_{ij,max}}\frac{\sigma_0^2}{E}dV \tag{8}$$

These equations define the contact patches between interacting grains (i and j) by determining the overlap of their order parameter fields through a geometric operation (Eq. (8)). By utilizing this approach, the simulation effectively captures the sintering process.

$$\Omega_{ij} = \begin{cases} \eta_i\eta_j\ , & \eta_i\eta_j \geq q \\ 0, & \eta_i\eta_j < q \end{cases} \tag{9}$$

The parameter q denotes the threshold that determines the required overlap for establishing contact between adjacent particles. Although the operation Ω_{ij} is traditionally utilized to identify grain boundaries, in the proposed model, it has been expanded to also identify particle contact. This extension enables the model to effectively capture the interactions between particles and accurately simulate their contact during the sintering process.

To obtain a normalized representation of the stress distribution within the contact, the order parameter fields in the overlap Ω_{ij} are normalized relative to the maximum value within that specific contact. This normalization is achieved by dividing Ω_{ij} by $\Omega_{ij,\max}$. Consequently, the function $\Omega_{ij}/\Omega_{ij,\max}$ serves as the discrete approximation of the normalized stress distribution within the contact. This approach allows for a consistent comparison and analysis of stress levels within different contact regions.

The peak stress in the center of a flake contact, σ_0, is calculated using the FEM simulation. Utilizing solid mechanics principles, an elastic model was employed in this study to induce pressure between two flakes. Considering the inevitable interaction between the flakes' surfaces upon collision, a penalty contact model was adopted to represent the interface between the flakes.

3. Results and discussion

Fig. 1(a) shows the original spherical shape of the Al powders with an average particle size of 10 μm. The SEM images of the Al powders after 3 h of BM are shown in Fig. 1(b), revealing a 2D planar morphology in the form of flaky particles with a thickness of 500 nm. Based on previous findings and our own published research [14,20], the Al flakes milled for 3 h were selected as the main constituents for the final Al/Al_2O_3 composite because of their well-defined flaky shape and intact structure without fragments. Moreover, the use of ethanol during BM resulted in individual platelets of the flake powder, which is beneficial for their alignment and consolidation in the composite. Fig. 2(a) shows the evolution of flake thickness and diameter to thickness ratio as a function of milling time. It can be observed that the Al flakes became thinner but more fragmented after 3 h of milling. In other words, the predominant

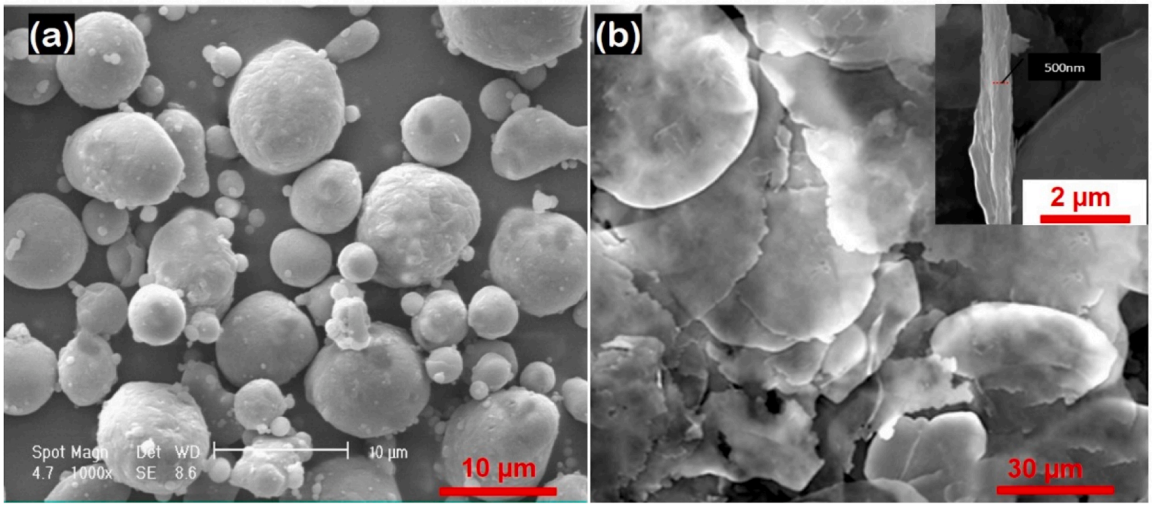

Fig. 1. SEM images of the (a) original spherical-shaped Al powder,(b) Flaky-shaped Al powder gained after 3 h BM, magnified image inside showing flake thickness of 500 nm.

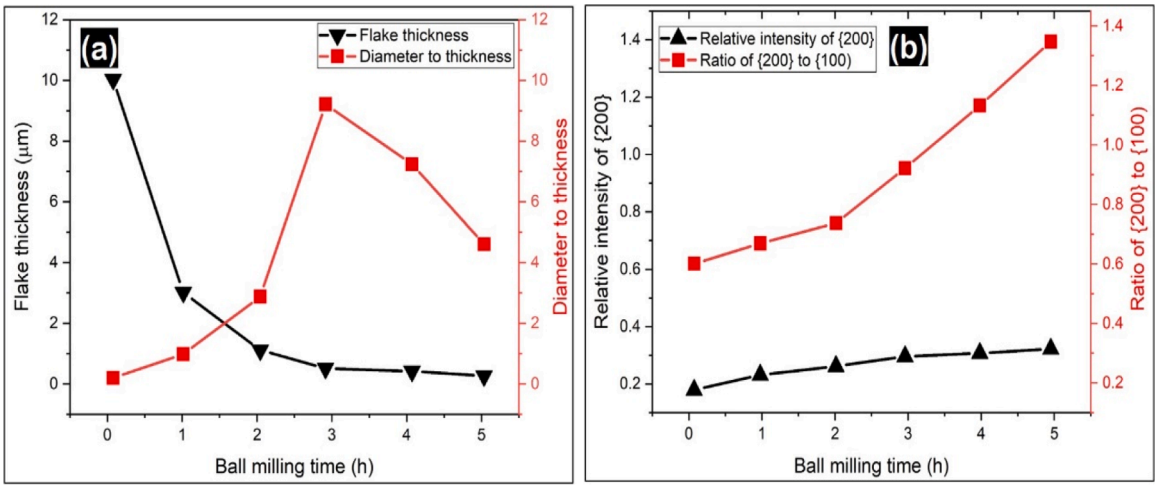

Fig. 2. (a) Variation of flake thickness and diameter to thickness with milling time from 0 h to 5 h. (b) Relative intensity of {200} plane and ratio of {200} intensity to {111} versus milling time.

deformation behavior during powder BM went from flattening to fragmentation at the 3-h mark. Consequently, the 3 h BM process resulted in ultrafine flakes with an approximate thickness of 500 nm and a diameter of 5 μm.

The diagram in Fig. 2(b) shows the relative intensity of the {200} planes and the ratio of {200} intensity to {111} at different milling times. Both the patterns and the curves in the graph show an upward trend of {200} intensity with increasing milling time, indicating that the BM process was similar to micro-rolling and resulted in a statistically preferred orientation of the Al flakes. In addition, other reasons, such as 1. the same type of deformation stresses, namely shear stresses, during the BM process and 2. the consideration of the milling balls as a conventional roller but on a smaller scale, can also be considered as similarities between micro- and macro-rolling [14,20]. During BM, an increase in the aspect ratio of the original grains together with cold welding of the particles contributed to the formation of high-angle grain boundaries (HAGBs) [29]. In fact, cold welding is a dynamic process of breaking and welding the as-milled Al flake powder is fractured and welded. The coalescence of the powder and the fracturing processes also change the shape of the powder particles.

Fig. 3 shows the microtopography of the cold-welded powders at different times. As can be seen in Fig. 3(a), after 15 min cold welding, the Al flakes were directly welded together without any obvious change in their shape. The welded particles were still flat and flaky, as shown in the magnified image in Fig. 3(b). In fact, after 1 h of cold welding, not only the bonding between the flakes can be improved, but also the Al_2O_3 fragments, which originally came from the natural skin on the Al particles, can be embedded both at the grain boundaries of Al and in the Al matrix, promoting the interfacial bonding between Al_2O_3 and the Al matrix. As the duration of cold welding increases, the strong shear and compressive stresses increase [30,31], so that the Al flakes were completely broken by the strong deformation and the broken pieces were rewelded, as shown in Fig. 3(c). The broken flakes can be clearly seen in Fig. 3(e). On the other hand, the cold welding reached a dynamic equilibrium after 2 h and relatively thick granules can be seen. This dynamic process caused the welded particles to be composed of more fragmented pieces and the overall shape of the particles changed from flakes to particles with a lamellar structure, so-called cake-like particles. The granules within a welded particle shown in Fig. 3(f) are much finer than the original Al flakes or the 1 h cold-welded powders.

Higher speed of milling provides intense collisions between the balls and the powder [32], which in turn generates a high impact energy on the powder, as the kinetic energy of the balls is transferred to the milled powder. Based on several models [33–36], the impact force during the

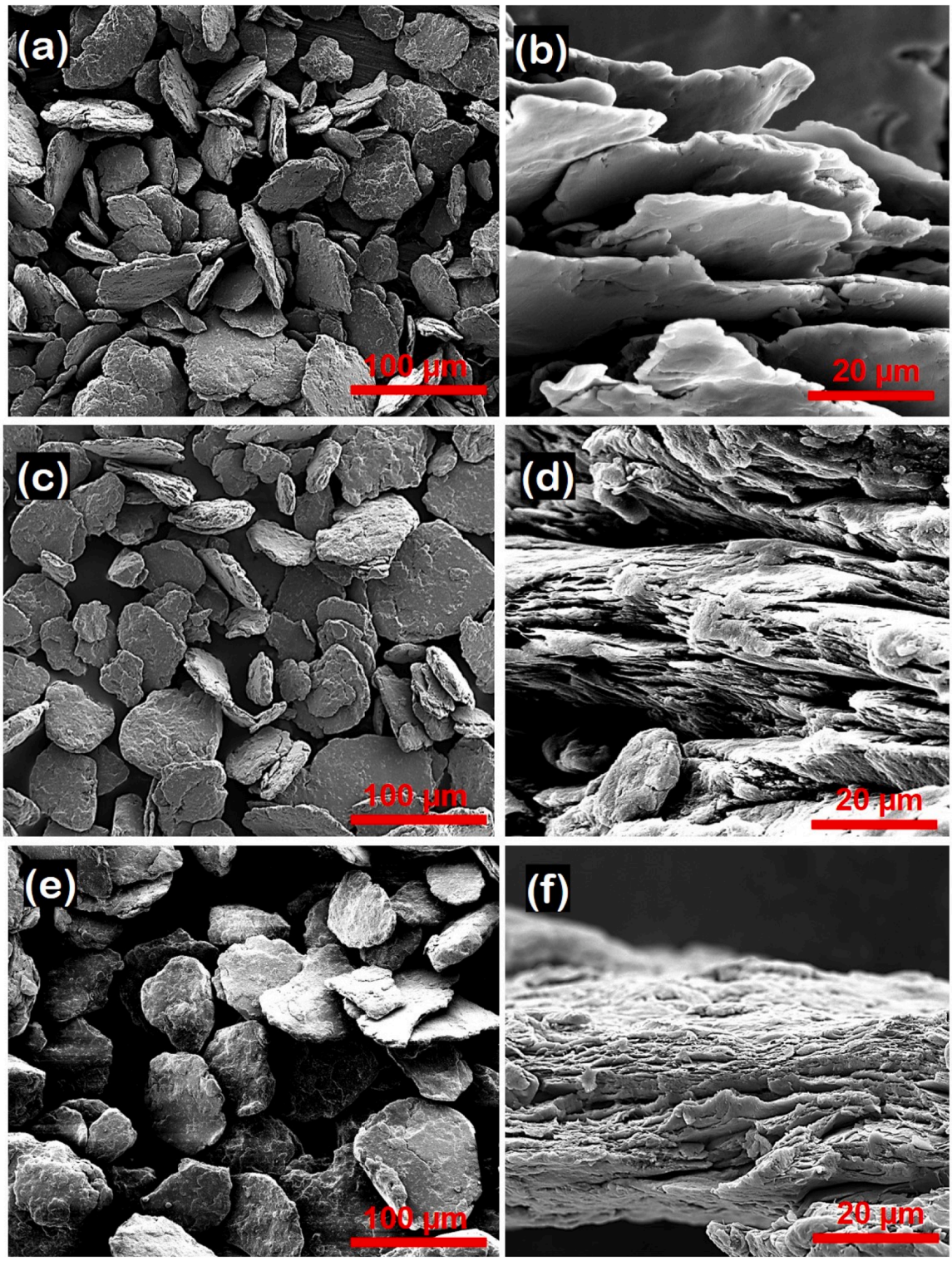

Fig. 3. SEM images of the cold welded particles with (a,b) 15 min, (c,d) 1 h, (e,f) 2 h of ball milling.

BM process can be divided into a radial component of compressive force and a tangential component of shear force. The most important factor in powder deformation, including flattening, cold welding and fragmentation, is the compressive force caused by the direct impact of the spheres [31,37,38]. In contrast, the shear force generated by the lateral impact, rotation of the balls and friction is considered to be an effective method for dispersing reinforcements [31,37,38]. Therefore, as the grinding speed increases, the compressive force, shear force and collision frequency would increase significantly, which in turn provides different growth rates, namely powder deformation and reinforcement dispersion. It was deduced that the proportion of the shear force increases significantly with longer time and higher speeds of the BM compared to the compressive force [31,39]. When the milling speed was doubled during high-speed BM (e.g. from 1 h to 2 h cold welding), both components of the collision force increased significantly, leading to an acceleration of powder flattening and cold welding. In addition,